

ON THE VIRIALIZATION OF DISK WINDS: IMPLICATIONS FOR THE BLACK HOLE MASS ESTIMATES IN AGN

AMIT KASHI¹, DANIEL PROGA¹, KENTARO NAGAMINE^{1,2}, JENNY GREENE³, AND AARON J. BARTH⁴

Draft version October 11, 2018

ABSTRACT

Estimating the mass of a supermassive black hole (SMBH) in an active galactic nucleus (AGN) usually relies on the assumption that the broad line region (BLR) is virialized. However, this assumption seems invalid in BLR models that consists of an accretion disk and its wind. The disk is likely Keplerian and therefore virialized. However, the wind material must, beyond a certain point, be dominated by an outward force that is stronger than gravity. Here, we analyze hydrodynamic simulations of four different disk winds: an isothermal wind, a thermal wind from an X-ray heated disk, and two line-driven winds, one with and the other without X-ray heating and cooling. For each model, we check whether gravity governs the flow properties, by computing and analyzing the volume-integrated quantities that appear in the virial theorem: internal, kinetic, and gravitational energies. We find that in the first two models, the winds are non-virialized whereas the two line-driven disk winds are virialized up to a relatively large distance. The line-driven winds are virialized because they accelerate slowly so that the rotational velocity is dominant and the wind base is very dense. For the two virialized winds, the so-called projected virial factor scales with inclination angle as $1/\sin^2 i$. Finally, we demonstrate that an outflow from a Keplerian disk becomes unvirialized more slowly when it conserves the gas specific angular momentum – as in the models considered here, than when it conserves the angular velocity – as in the so-called magneto-centrifugal winds.

Keywords: accretion, accretion disks — hydrodynamics — methods: numerical — (galaxies:) quasars: general

1. INTRODUCTION

Many astrophysical systems in equilibrium are virialized. Examples range from objects that are in hydrostatic equilibrium, such as stars, planets, and intergalactic medium, to dynamical systems such as planetary systems, binary stars, stellar globular clusters, and galaxies. For such systems, the mass inside a sphere of a radius r and a characteristic velocity v are related through the well known equation

$$M(< r) = f \frac{rv^2}{G}, \quad (1)$$

where f is a factor that depends on the geometry and dynamics, and G is the gravitational constant. For example, in the case of Keplerian rotation, $f = 1$ because the gravity and centrifugal forces are equated, while in the case of supersonic accretion, $f = 0.5$ because the gravitational potential energy and kinetic energy are equated. For such simple cases, f does not change when it is integrated over some volume, even if weighted by a non-uniform density. If the system is more complicated, the density-weighted, volume-integrated f could be dominated by the denser part of the flow.

It is often assumed that the broad line regions (BLRs)

in active galactic nuclei (AGN) are also virialized. This assumption cannot be directly verified because the BLRs are spatially unresolved. However, the very compactness of the BLRs and the broadness of the observed lines suggest that the dynamics of the BLR gas is strongly coupled to the gravity of the central supermassive black hole (SMBH). Therefore, the assumption of virialization has been used to determine the SMBH mass M_{BH} , provided both v and r are known. In the case of AGN, practically all the mass is concentrated in the center with M_{BH} being much greater than that of stars and gas, therefore $M(< r) = \text{constant} = M_{\text{BH}}$. The emission line width, Δv , can be measured relatively easily and used as an estimate of v . Using reverberation mapping, the distance r can be estimated via $r = c\tau$, where τ is the time delay for BLRs to respond to changes in the continuum (e.g., Blandford & McKee 1982; Peterson 1993). This method has been used in many AGN surveys for multiple emission lines with different characteristic emission radii, and it has been improved over the years (e.g., Ulrich et al. 1997; Peterson & Wandel 1999, 2000; Peterson 2001,2004; Kaspi et al. 2000; Kollatschny 2003; Bentz et al. 2009; Pancoast et al. 2011; Hryniewicz & Czerny 2012; Shen 2013; Barth et al. 2013). It has also been suggested that the BLRs are virialized based on the correlation between the time delay and line width (e.g., Peterson & Wandel 1999, 2000; Onken & Peterson 2002; Kollatschny 2003; Peterson et al. 2004).

Although the basic assumptions behind the above mentioned method are very plausible, the method has its limitations. For example, different BLR structures, the radiation pressure, viewing angle, gravity due to

¹ Department of Physics & Astronomy, University of Nevada, Las Vegas, 4505 S. Maryland Pkwy, Las Vegas, NV, 89154-4002, USA kashia@physics.unlv.edu

² Department of Earth and Space Science, Graduate School of Science, Osaka University, 1-1 Machikaneyama-cho, Toyonaka, Osaka, 560-0043, Japan

³ Department of Astrophysical Sciences, Princeton University, Princeton, NJ 08544, USA

⁴ Department of Physics and Astronomy, University of California, Irvine, Irvine 92697, CA, USA

the host galaxy, and different methods for characterizing the broad-line widths are all expected to affect the measurements (e.g., Krolik 2001; Watson et al. 2007; Marconi et al. 2008; Gaskell 2010; Goad et al. 2012; Denney 2012). Due to these systematic effects, the value of f may be uncertain by two orders of magnitude (e.g., Krolik 2001). Observations have estimated the average values in the range of $\langle f \rangle \approx 1\text{--}6$ (McLure & Dunlop 2004; Onken et al. 2004; Woo et al. 2010; Grier et al. 2013).

Observational estimates of the value of f may differ from the theoretical ones. In some cases, the value of f used by observers is composed of a correction factor which depends on the definition of the line width, and a theoretical factor which assumes some geometry and dynamics.

Another issue with this method is that the relation $r \propto v^{-2}$, which comes from the virial assumption (Eq. 1), can hold not only in virialized systems, but also in several types of winds (Krolik 2001). On the other hand, winds have been proposed as one of the possible scenarios for the BLR in AGNs, and have been studied extensively both observationally and theoretically (e.g., Kallman et al. 1993; Arav et al. 1994; Konigl & Kartje 1994; Murray et al. 1995; Chiang & Murray 1996; Nicastro 2000; Laor et al. 2006; Bentz et al. 2010; Sim et al. 2010; Wang et al. 2011; Roth et al. 2012; Kollatschny & Zetzl 2013).

A closely related question is how observations of a certain emission line can tell us whether the system is virialized or not. Richards et al. (2011) showed that a number of different emission-line features are consistent with a two-component disk+wind model of the BLR (e.g., Collin-Souffrin et al. 1988; Leighly 2004). Baskin & Laor (2005) found that, while the most widely used H β line is virialized, the second most used CIV line has a non-virialized component (but see Denney et al. 2013 for recent contradicting results). This may suggest that virialization can be limited to only some parts of the BLRs.

These considerations motivate us to check whether the outflows could be virialized and if so to what extent. In this paper, we analyze four simulations of different *disk wind* models, and examine which parts of the winds are virialized. In §2, we briefly describe the simulations that we analyze. In §3, we describe our analysis methods. In §4, we present our analysis results. In §5, we discuss how an outflow from a virialized Keplerian disk becomes unvirialized. A summary of our findings is given in §6.

2. SIMULATIONS

Here, we analyze four different axisymmetric two-dimensional (2-D) Eulerian hydrodynamic simulations of winds driven off disks that accrete onto a central object. These simulations are chosen from the earlier works by Proga and his collaborators to provide controlled environments, representing different aspects of winds driven from a Keplerian accretion disk. We chose these four particular simulations in order to explore disk winds with different physics not because they are necessarily the best to model the BLRs. In fact, only the last simulation has been performed with parameters suitable for quasars and captures the minimum required physics. However, the first three simulations are relevant in the context of this paper because they can be rescaled to AGN (see below

for scaling relationships). In addition, as we show, they are useful to understand and highlight the properties of the wind in the fourth simulation and assess its generality. Specifically, the first two simulations illustrate that not all disk winds appear to be virialized and emphasizes that the size of the acceleration zone is the key to wind virialization. Table 1 compares the physics included in each model. Below we give brief descriptions of each model.

Model 1: An isothermal, steady state, wind model B from Giustini & Proga (2012). This model is one of several tests computed by Luketic et al. (2010). In this, perhaps simplest, disk wind models, the gas expands and accelerates because it is implicitly heated (gains energy) in accordance with the assumption of being isothermal. The calculations and results are presented in units where $GM = 1$ and the sound speed $c_s = 1$ (i.e., distance is in units of $r_0 = GM/c_s^2$). As found by Font et al. (2004), the geometry of such winds depends on the density profile along the equator: flat profiles yield vertical winds whereas the profiles where the density decreases strongly with radius yield spherical winds (see also Giustini & Proga 2012 for more details). Here, we present the results for the density profile $\rho \propto r^{-2}$ that produces a nearly spherically symmetric wind. The ratio between the maximum velocity at the end of the computational domain and the Keplerian velocity at $r = 1$ (in the simulation units) is $v_{\text{out,max}}/v_K(r = 1) = 3.57$ for this model. This ratio is an indicator of the wind acceleration and virialization: lower values indicate weak acceleration (the gravity is dominant) whereas high values suggest very strong acceleration resulting in an unvirialized outflow. A value of more than 3, as in model 1, indicates an unvirialized outflow. This is confirmed by our more detailed analysis summarized below in §4.

Model 2: A thermal wind model from an X-ray heated disk, which is similar to the model C8 of Luketic et al. (2010), but with an outer radius 5 times greater. The BH mass in this model is $M = 7M_\odot$, and the total luminosity is $L_{\text{tot}} = 0.03L_{\text{Edd}}$, where L_{Edd} is the Eddington luminosity (therefore the wind cannot be driven by radiation pressure). The adiabatic index is $\gamma = 5/3$. The density profile is $\rho = 10^{-11}(r/r_{\text{IC}})^{-2} \text{ g cm}^{-3}$, where $r_{\text{IC}} = GM\mu m_p/(k_B T_{\text{IC}}) = 4.8 \times 10^{11} (M/7M_\odot) (\mu/0.6) (T_{\text{IC}}/1.4 \times 10^7 \text{ K})^{-1} \text{ cm}$ is the inverse-Compton (IC) radius. The distance for this model is in units of r_{IC} . We note that the units for the Model 1 and 2 are related to each other by $r_{\text{IC}} = r_0 = GM/c_s^2$. As Model 1 is a simplest example of a thermally driven disk wind, Model 2 can be viewed as a more physical variate of Model 1 because in Model 2 the physics of gas heating and cooling is explicitly included. One of the consequences of this more physical model is that here the wind solution does not depend on the density profile as long as the density is high and the gas temperature is low. This model includes radiation heating and cooling, as applied in Proga & Kallman (2002) and Proga et al. (2000). The local X-ray flux is corrected for optical depth effects, taking only electron-scattering as the source of opacity. This model produces a fast-moving (few $\times 100 \text{ km s}^{-1}$) high-density wind with convex streamlines close to the

Table 1

Comparison of physics in the simulations analyzed in this work. References: Model 1. Giustini & Proga (2012); Model 2. Luketic et al. (2010); Model 3. Proga (2003); Model 4. Proga & Kallman (2004).

Model	Gravity	Rotation	Radiative gas heating and cooling	Radiation pressure	Equation of state	$L_{\text{tot}}/L_{\text{Edd}}$	Units of distance
1	Yes	Yes	No	No	Isothermal	0	GM/c_s^2
2	Yes	Yes	Yes	No	Adiabatic	0.03	GM/c_s^2
3	Yes	Yes	No	Yes	Isothermal	0.0015	$r_{\text{WD}} = 8700 \text{ km}$
4	Yes	Yes	Yes	Yes	Adiabatic	0.6	$2GM/c^2$

poles and slower ($\text{few} \times 10 \text{ km s}^{-1}$) concave streamlines close to the equator. The $v_{\text{out,max}}/v_{\text{K}}(r=1)$ ratio is 1.50 indicating that the acceleration is weaker compared to model 2.

Model 3: A line-driven disk wind model E2 from Proga (2003) (see also Proga et al. 1998). In this model thermal driving is negligible, the driving is not due to gain of thermal energy but due to transfer of momentum from radiation to the gas. As such, compared to Model 1 and 2, Model 3 represents a physically different class of winds. The model assumes a disk around a $0.6M_{\odot}$ white dwarf (WD) of radius $r_{\text{WD}} = 8700 \text{ km}$ with an isothermal equation of state. We show this particular model because it quite well accounts for observations of disk winds in cataclysmic variables (see fig. 2 in Proga 2003) and has been used as a base for disk winds in AGNs (see below). Distances in this model are expressed in units of r_{WD} . The total luminosity of the accretion disk and WD is $L_{\text{tot}} = 1.5 \times 10^{-3} L_{\text{Edd}}$. The model computes the radiation force due to lines using the intensity of the radiation integrated over the UV-band only. The density profile in the disk is $\rho = 10^{-9}(r/r_{\text{WD}})^{-2} \text{ g cm}^{-3}$. The model calculates the line force that drives winds from a thin disk based on Proga et al. (1999). The resulting outflow shows radial streamlines with very high velocities ($\text{few} \times 10^3 \text{ km s}^{-1}$) in high latitudes and very low ($\text{few} \times 10 \text{ km s}^{-1}$) velocities at low latitudes. Here, the $v_{\text{out,max}}/v_{\text{K}}(r=1)$ ratio is 1.99. Rescaling results from Model 3 to AGN is not straightforward, in part because it does not include some of the physical processes that are essential in AGN, e.g., the X-ray ionization. Therefore, our last model is an extension Model 3 that was computed specifically for AGN.

Model 4: A line-driven wind with X-ray heating and cooling (Proga & Kallman 2004). The model describes a wind from a disk around a $M = 10^8 M_{\odot}$ SMBH. The distance in this model is given in units of the Schwarzschild radius $r_s = 2GM/c^2 = 3 \times 10^{13} \text{ cm}$. The disk luminosity is $L_D = 0.5L_{\text{Edd}}$, and the luminosity of the central engine is $L_c = 0.1L_{\text{Edd}}$ with 90% of the radiation in the UV and 10% in the X-ray. The model computes the radiation force due to lines using the intensity of the radiation integrated over the UV-band only. The central engine produces photons that can ionize the gas, but its contribution as a source of radiation pressure was excluded. The adiabatic index is $\gamma = 5/3$. The gas density along the disk midplane was assumed to scale as $\propto r^{-2}$. For small radii at the disk atmosphere and wind base, the model predicts a typical density $\sim 10^{-12} \text{ g cm}^{-3}$ which results in a relatively low photo-ionization param-

eter ($\log \xi < -5$) despite the strong radiation coming from the center. In addition, the model predicts significant self-shielding: dense clumps form close to the center (“failed wind”) as a result of the over-ionization, which provide shielding for the gas launched at large radii. The disk wind is very fast ($\sim 10^4 \text{ km s}^{-1}$) at low latitudes whereas at high latitudes, there is a low density inflow. Here, the $v_{\text{out,max}}/v_{\text{K}}(r=1)$ is 0.13. As shown by Proga & Kallman (2004) this class of models well accounts for the properties of outflows observed in broad absorption line quasars (see also Sim et al. 2010, and references therein).

3. ANALYSIS METHODS

The simulations described above solve either hydrodynamic or radiation+hydrodynamic equations in an Eulerian form on a 2-D grid with axial symmetry. The wind solution is given as the spatial distribution of local quantities as a function of time. These quantities are the density ρ , specific internal energy e , and velocity \mathbf{v} . Therefore the simulations provide all the necessary information to compute the terms of the virial equation

$$\Phi_G = -2(E + K), \quad (2)$$

where Φ_G , E and K are the density-weighted, volume-integrated quantities of gravitational potential $\phi_G = GM/r$, specific internal energy, and specific kinetic energy $k = v^2/2$, respectively.

For Models 1–4, we compute the terms in the virial theorem. These models assumed axial symmetry, however, the rotational component of velocity v_{φ} was implicitly calculated, and it is used in our analysis. Following the original papers that presented the simulations, we use spherical polar coordinates.

We calculate the kinetic component of the virial factor

$$f_k = \frac{|\phi_G|}{2k} \quad (3)$$

as a function of position. When $e \ll k$, f_k measures where the flow is close to or largely deviating from virialization. In this case $f_k \simeq 1$ would indicate a virialized region in the flow. We note that in some cases e can be dominant, for example, in stellar interiors.

We calculate the density-weighted, surface-integrated virial quantities using the following equation:

$$\tilde{q}_i = \int_{\varphi=0}^{2\pi} \int_{\theta=0}^{\pi} q_i \rho^n \sin \theta \, d\theta \, d\varphi, \quad (4)$$

where $q_i = (\phi_G, e, k)$, and they are weighted by ρ^n . To

examine the effects of winds on observations, we take $n = 1$ for continuum fluorescence excitation line emission, and $n = 2$ for recombination line emission and collisionally excited line emission.

Finally, we compute the density-weighted, volume-integrated quantities

$$Q_i = \int_{\varphi=0}^{2\pi} \int_{\theta=0}^{\pi} \int_{r=0}^r q_i \rho r^2 \sin \theta dr d\theta d\varphi, \quad (5)$$

where $Q_i = (\Phi_G, E, K)$ for $q_i = (\phi_G, e, k)$, respectively. Also, $K = (K_r, K_\theta, K_\varphi)$ are the radial, meridional, and rotational components of K , respectively.

We use the local properties of the wind to check if k scales with radius the same way as ϕ_G , namely, if f_k is radius independent. If f_k is constant, then it means that Equation (2) will hold and the system is virialized. But even if it is not constant, Eq. (2) can still hold when the density-weighted volume integral is performed, and the system is virialized.

In Appendix A, we illustrate the results of our analysis on the well known Bondi accretion flow (Bondi 1952) and Parker wind (Parker 1965). We will use these results to compare with more complicated cases in the following sections.

4. RESULTS

In the following, we present three sub-figures for each simulation, and each sub-figure contains a few panels. The *sub-figure (a)* presents the following flow properties: the density map (left most panel), the poloidal velocity field (second left panel), the comparison of radial and rotational velocities (v_φ/v_r ; third panel), and f_k (right-most panel). Note that the abscissa of sub-figure (a) is using $r' = r \sin \theta$.

The *sub-figure (b)* presents the ratio of gravitational potential and kinetic energy $2\tilde{k}/\tilde{\phi}_G$, weighted by ρ^n and surface-integrated (see Eq. [4]). We are presenting its components in order to show the contribution of each component separately. The left panel shows the ratios for the total kinetic energy with $n = 0, 1, 2$, whereas the right panel shows the radial, meridional and rotational components.

Finally, the *sub-figure (c)* presents the volume-averaged properties of the flows. The left panel presents the quantities $2Q_i/|\Phi_G|$ (Eq. [5]), which relate to each component of the inverse virial factor. We define the density-weighted, volume-integrated virial factor

$$\mathfrak{f} = \frac{|\Phi_G|}{2(E + K)}, \quad (6)$$

as an analogue of the non-density weighted integrand f , which is also shown in the left panel by the dashed gray line. The theoretical value of \mathfrak{f} is 0.5 for supersonic accretion, and 1 for Keplerian rotation. The same panel also shows M_g/M_{tot} , the total gas mass within a radius r , normalized by the total mass (green solid line). In the middle and right panels, we present the projected radial and rotational components of the kinetic energy $K_{r,p}$ and $K_{\varphi,p}$ respectively, as viewed at an angle i , measured from the pole.

We emphasize that the ultimate indication for a flow to be virialized is that \mathfrak{f} has a flat radial profile, because these components (density-weighted, volume-integrated internal energy, kinetic energy and gravitational potential) are the quantities that enter the virial theorem.

Figure 1 presents the results of Model 1 (the isothermal wind). Figure 1a shows that the radial component dominates over the rotational component everywhere except for near the equator. The right panel shows that f_k is a function of r , but a very weak function of θ . It is evident that at $r \gtrsim 1$ the flow is highly non virialized for every θ .

Figure 1b shows that the radial component of \tilde{k} becomes dominant at $r \gtrsim 0.5$, independent of the value of n . This transition radius is expected, because the density becomes close to spherically symmetric at greater radii, and thus the integration does not affect the value of \tilde{k} (Eq. [4]).

Figure 1c reveals four significant properties of the isothermal wind: (i) The rotational component K_φ is dominant up to $r \simeq 1$, and beyond this radius K_r becomes dominant. (ii) The flow is not virialized, mainly due to the large values of K_r . (iii) The projected component $K_{r,p}$ varies very little as a function of a viewing angle. Again this is expected, because the wind is close to spherically symmetric, and the velocity field is dominated by the radial component. (iv) The projected component $K_{\varphi,p}$ varies as a function of a viewing angle, because v_φ is not spherically symmetric. We find that the kinetic properties of the flow do not scale with the gravitational potential, independent of the density weighting and viewing angle. This indicates that, for the isothermal wind model, the outflow would be observed as non-virialized in resonance and recombination lines from any viewing angle.

Figure 2 shows the results for Model 2 (thermal wind from an X-ray heated disk). The right panel of Figure 2a shows that f_k is a strong function of r and θ . Therefore it is not straightforward to draw conclusions about the virialization of the flow using this information alone, though the large volume with blue and purple colors ($f_k \ll 1$) hints that this is not a virialized flow. It requires our analysis of density-weighted, surface and volume integrated quantities to verify that the flow is not virialized.

Figure 2b shows that for Model 2, the radial range where the rotational component is dominant depends on n . For $n = 0$ and 1, the radial part becomes important at $r \gtrsim 1$, while for $n = 2$ the rotational component dominates up to the outer computational domain of $r = 100$.

From the left panel of Figure 2c, we learn that the flow is virialized in the inner region of $r \lesssim 2$ (see the dashed gray line), in which point the radial component becomes more important than the rotational component. The rotational component originates from the Keplerian disk, and it makes the flow virialized. One can say that the wind “remembers” its attachment to the central object up to that radius. We conclude that the wind in Model 2 would be observed as non-virialized, because it is virialized only in the inner regions.

Figure 3 present the results of Model 3 (line-driven wind). Figure 3a shows that f_k varies significantly as a function of θ , but is only a weak function of r . More importantly, a large volume ($\theta \gtrsim 40^\circ$, for all r) has $f_k \sim 1$

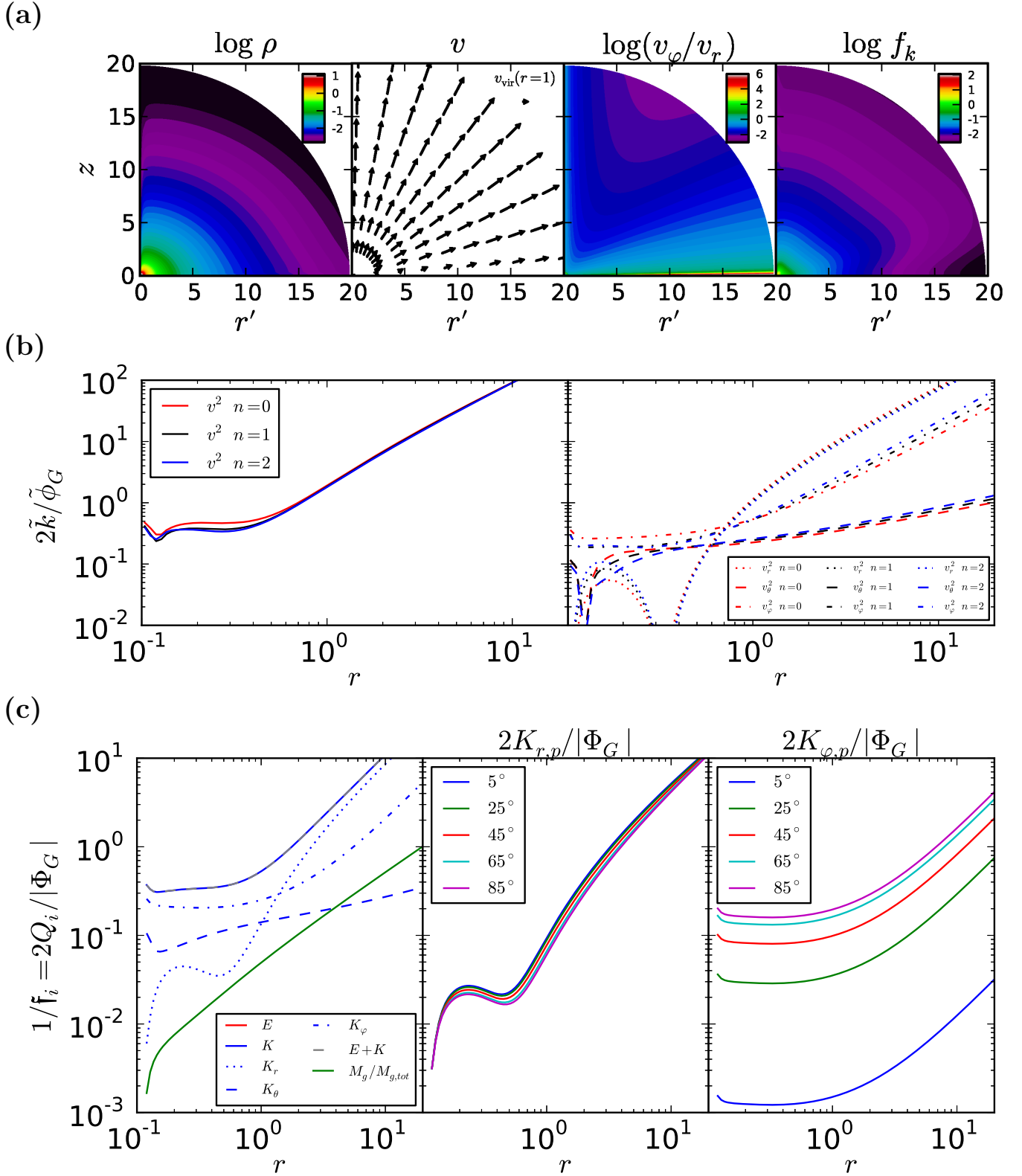


Figure 1. For Model 1 (isothermal wind). **Subfigure (a):** The flow properties are computed and presented in units where $GM = 1$. *Left panel:* The density map. *Second Panel:* The poloidal velocity field. *Third panel:* the ratio between the rotational and radial components of the velocity. Note the rapid change close to the equator ($\theta = 90^\circ$) where the rotational component dominates. *Right panel:* The parameter f_k (Eq. [3]). **Subfigure (b):** *Left panel:* the ρ^n -weighted and surface-integrated kinetic energy, normalized by the gravitational potential. *Right panel:* The components of the density-weighted and surface-integrated kinetic energy, normalized by the gravitational potential. The components that appear in the legend but not in the figure (or in the figure partially) have lower values than the lower limit of the ordinate, and are negligible compared to the others. **Subfigure (c):** *Left panel:* Inverse of various virial factors $\tilde{f}_i^{-1} = 2Q_i/|\Phi_G|$ (Eq. [5]), where Q_i are the internal energy E , the total kinetic energy K , and its components K_r , K_θ and K_ϕ . Also plotted is $M_g/M_{g,\text{tot}}$, the normalized, integrated gas mass contained within radius r . The dashed-gray line gives the value of \tilde{f}^{-1} (Eq. [6]) as a function of radius. Note that it overlaps with the blue line (K) as $E \ll K$ (E is below the lower limit of the ordinate). The value of \tilde{f} is the important value for determining if the flow is virialized. Here it is not flat and reaches values $\ll 1$, therefore the flow is not virialized. The middle and right panels show the projected quantities K_r and K_ϕ , respectively, observed from viewing angles i , measured from the pole (see legend).

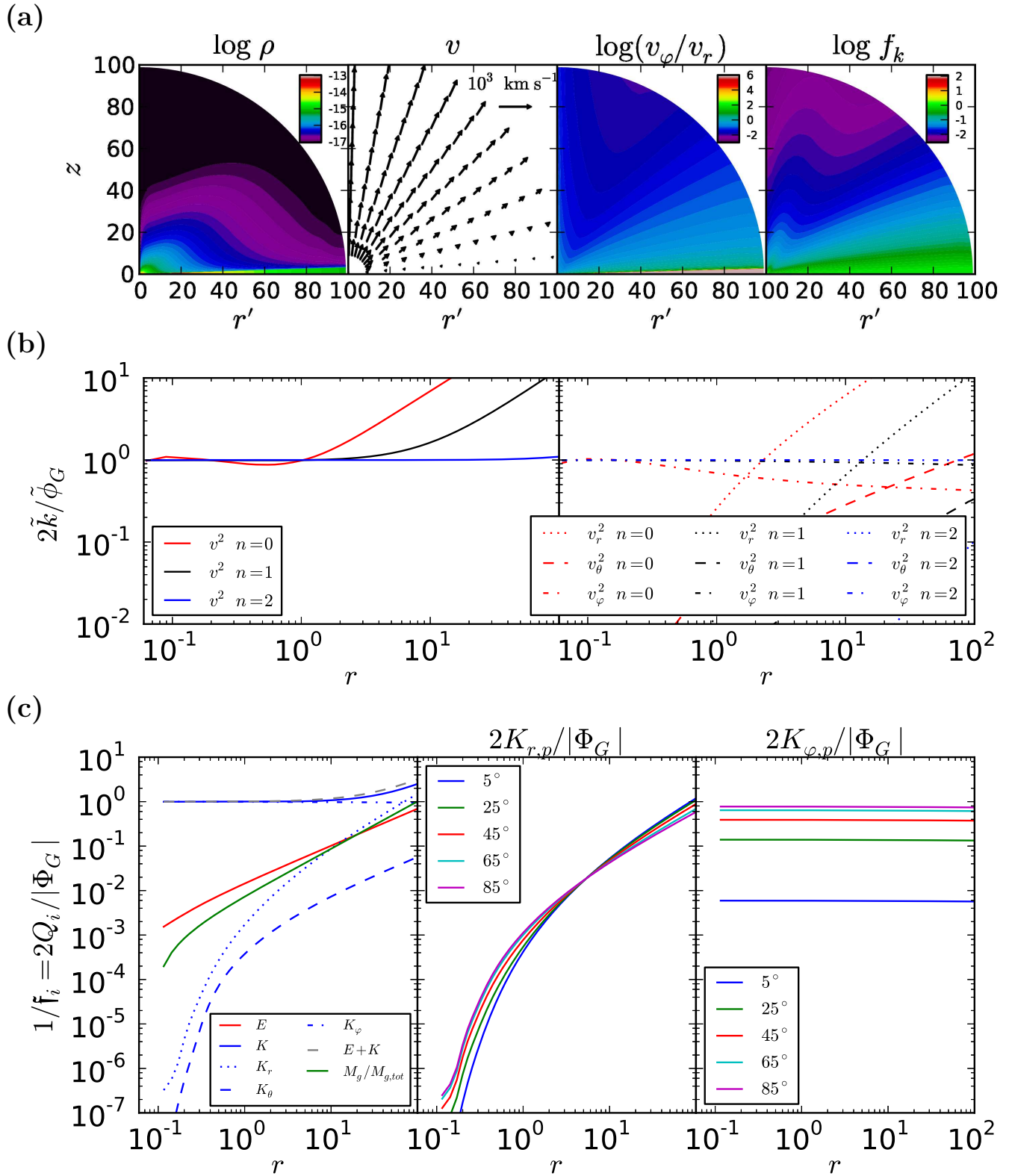


Figure 2. Same as Fig. 1, but for Model 2. The distance for this model is in units of the inverse Compton radius r_{IC} . Note that $r' = r \sin \theta$.

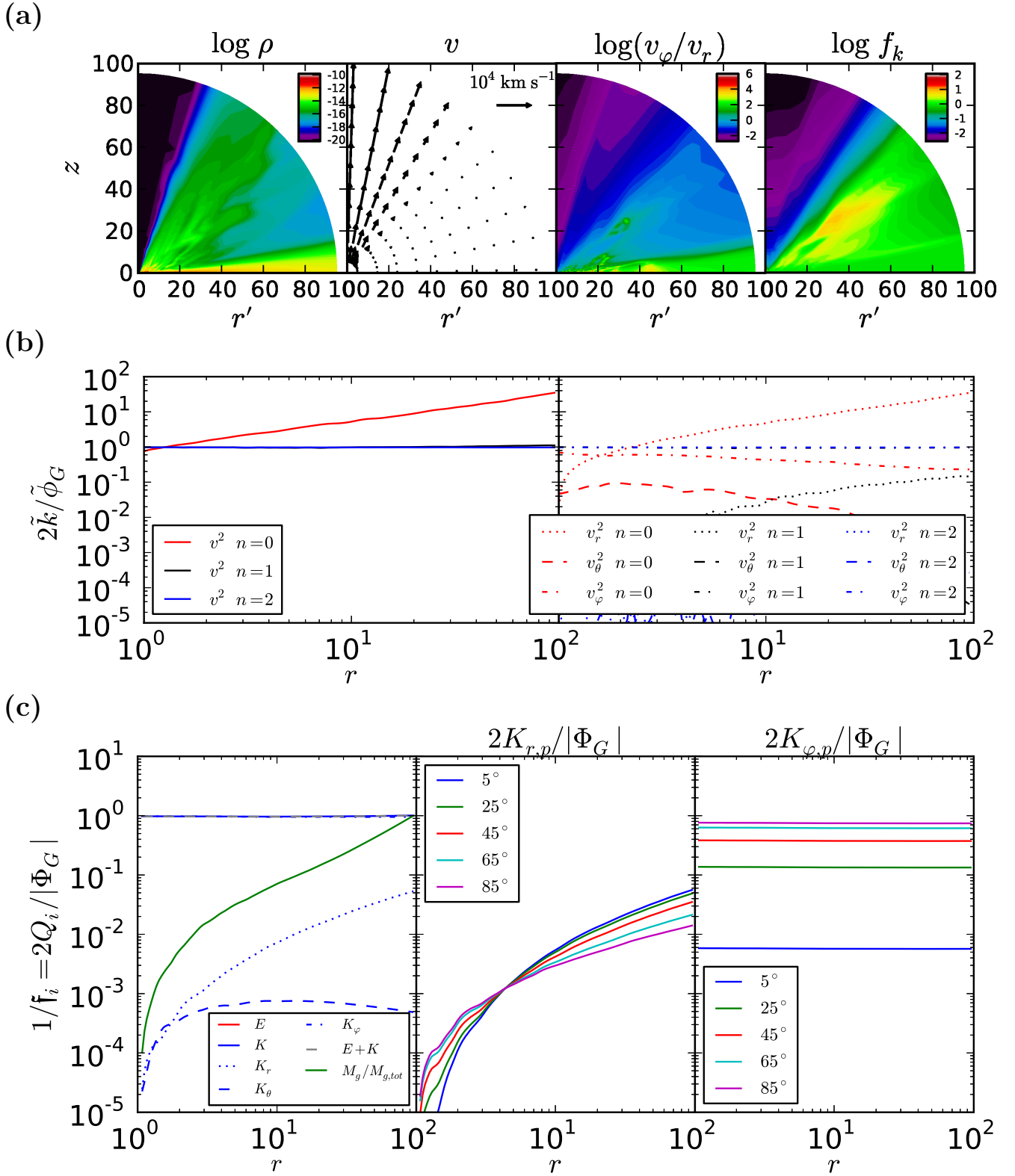


Figure 3. Same as Fig. 1, but for Model 3. The distance for this model is in units of white dwarf radius r_{WD} . Note that, in the left panel of sub-figure (c), the dashed-gray line (f) overlaps with the blue line (K) as $E \ll K$, and with the dotted-dashed blue line K_φ , because $K_\theta, K_r \ll K_\varphi$. The value of f is flat, therefore we conclude that for this model the flow is virialized.

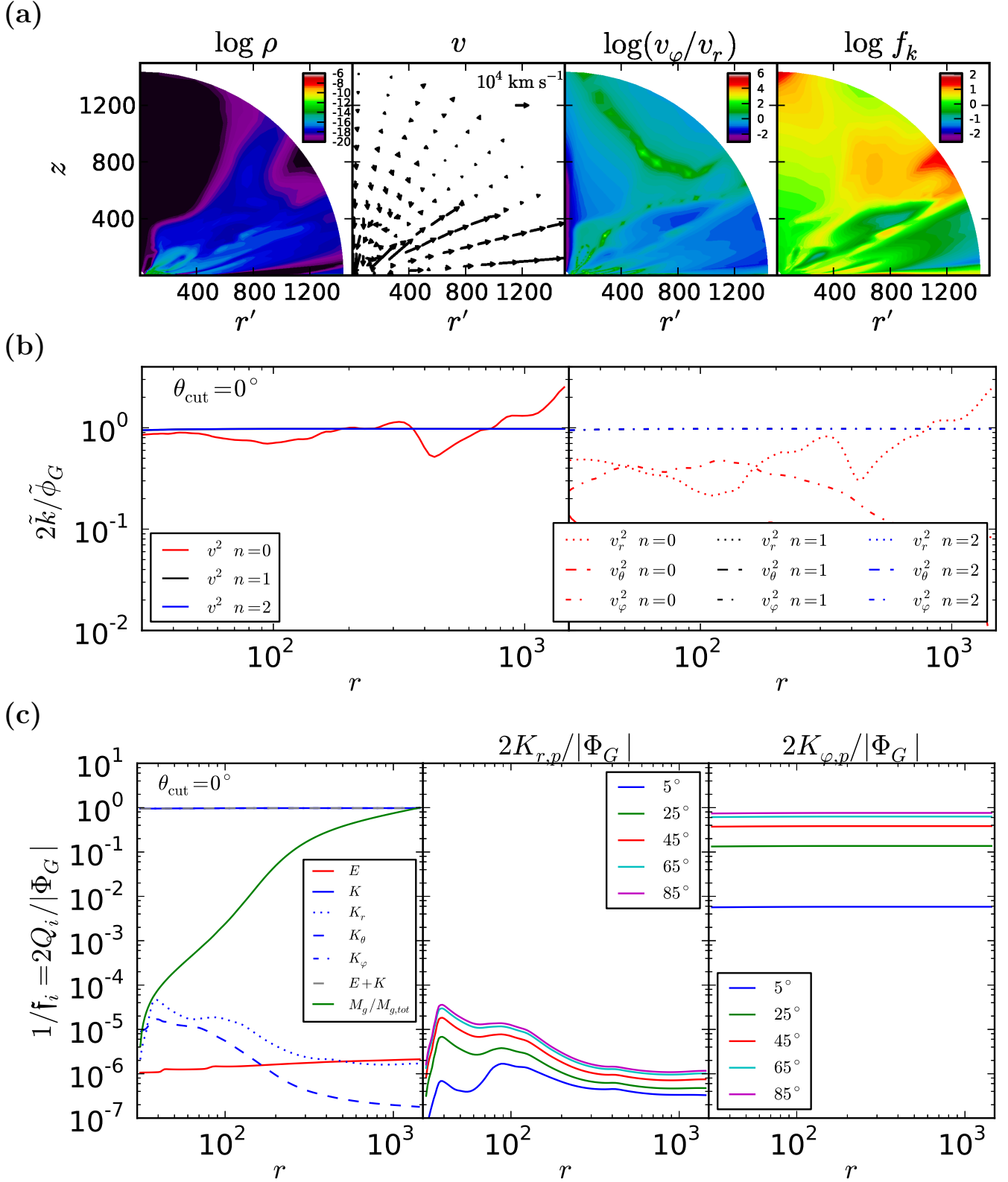


Figure 4. Same as Fig. 1, but for Model 4. The distance for this model is given in units of the Schwarzschild radius $r_s = 2GM/c^2 = 3 \times 10^{13}$ cm. Note that in the left panel, the dashed-gray line (f) overlaps with the blue line (K) because $E \ll K$ (E is below the lower limit of the ordinate), and with the dotted-dashed blue line K_φ because $K_\theta, K_r \ll K_\varphi$. The value of f is flat, therefore we conclude that for this model the flow is virialized.

(shown in green-to-yellow colors), which indicates that the flow is virialized. The left-most panel shows that this region is the denser part of the flow.

Figure 3b shows that for this model, similarly to the Model 2, the radial range where the rotational component dominates depends of n . For $n = 0$, the radial component dominates, and the kinetic component does not scale with gravity, while for $n = 1$ and 2 the rotational component dominates up to the outer computational domain of $r = 100$.

Figure 3c shows that for this model, the flow is completely virialized up to the radial boundary. The right panel shows that $K_{\varphi,p}/|\Phi_G|$ is almost independent of radius. The actual value of $K_{\varphi,p}/|\Phi_G|$ scales as $\propto \sin^2 i$. We find that $K_{\varphi,p} > K_{r,p}$ for viewing angles $i \gtrsim 20^\circ$. We conclude that for Model 3, the wind would be observed as virialized for viewing angles $i \gtrsim 20^\circ$.

Figures 4 presents the results of Model 4 (line-driven wind with X-ray heating and cooling). In the left panel of Figure 4a, we see a dense region near the center (colored in green) that corresponds to the failed wind. The right panel shows that $f_k \sim 1$ in most of the volume.

Figure 4b shows similar results to Model 3 with regard to the dominance of the radial and rotational components. According to Figure 4c, the flow is completely virialized up to the edge of the computational domain ($r = 1500$). This translates to $\sim 4.5 \times 10^{16}$ cm for a SMBH with $10^8 M_\odot$. It is clearly seen that K_φ is the dominant component. The right panels show that $K_{\varphi,p}/|\Phi_G|$ remains flat for any line of sight, and that $K_{\varphi,p} > K_{r,p}$ for any value of θ . The scaling $K_{\varphi,p}/|\Phi_G| \propto \sin^2 i$ is the same as in Model 3. This suggests that the system would be observed as virialized from any line of sight.

Analyzing Models 3 and 4, we find that, in the regions where the wind is virialized, the scaling of f_p with the inclination angle is

$$f_p \equiv |\Phi_G|/K_p = \frac{1.32 \pm 0.08}{\sin^2 i}. \quad (7)$$

Another issue in testing the virialization of winds is the separation of winds from the dense disk. As a test, we repeat the same calculation after excluding the equatorial region with $\pi/2 + \theta_{\text{cut}} < \theta < \pi/2 - \theta_{\text{cut}}$ as follows:

$$Q_i = \int_{\varphi=0}^{2\pi} \int_{\theta=0}^{\pi/2-\theta_{\text{cut}}} \int_{r=0}^r q_i \rho r^2 \sin \theta dr d\theta d\varphi + \int_{\varphi=0}^{2\pi} \int_{\theta=\pi/2+\theta_{\text{cut}}}^{\pi} \int_{r=0}^r q_i \rho r^2 \sin \theta dr d\theta d\varphi. \quad (8)$$

We performed this test for Models 3 and 4, and found that the winds are virialized in both of cases. Here we show only the results for Model 4 as an example of this test. Figure 5 shows the result of Model 4 with $\theta_{\text{cut}} = 5^\circ$ (top row) and $\theta_{\text{cut}} = 25^\circ$ (bottom row). This emphasizes the significance of high-density wind near the center, which is shown in the left panel of Figure 4a in green. When the integrated quantities are weighted by density, it is seen that the wind itself is virialized, because $f \simeq 1$ even for $\theta_{\text{cut}} = 25^\circ$.

5. DISCUSSION: UNVIRIALIZATION OF AN OUTFLOW

To illustrate how a Keplerian flow becomes unvirialized due to an outflow, we use the following analytic calculation. We consider a gas element outflowing from a point ($r' = r'_0, z = 0$) on the equator where the Keplerian velocity is $v_k = (GM/r'_0)^{1/2}$. A new position of the element (r'_1, z_1) can be expressed by the distance l from the original location and the inclination angle α measured from the equator (see top panel of Figure 6). As a result of specific angular momentum conservation, the rotational velocity of the gas at the new location would be $v_\varphi = (r'_0/r'_1)v_k$. We can calculate $f_{k,\varphi} = |\phi_G|/v_\varphi^2$, the rotational component of f_k , as a function of l and α :

$$f_{k,\varphi} = \frac{(r'_0 + l \cos \alpha)^2}{r'_0 [(r'_0 + l \cos \alpha)^2 + (l \sin \alpha)^2]^{1/2}}. \quad (9)$$

The solid lines in the bottom panel of Figure 6 show $f_{k,\varphi}$ as a function of l for different values of α , for a launching point of $r'_0 = 1$. One can see that generally $f_{k,\varphi}$ is a weak function of l . For example, at $l = 10$, $f_{k,\varphi}$ varies by a factor of ~ 1.5 at most for $\alpha = 70^\circ$, and increases by a factor of ~ 11 for $\alpha = 10^\circ$,

We also check another type of flow, where the conserved quantity is not the angular momentum but instead the angular velocity, as in the so-called magnetocentrifugal winds (Blandford & Payne 1982). In this case, $v_\varphi = (r'_1/r'_0)v_k$. As an analogue of $f_{k,\varphi}$, we calculate

$$f_{k,\varphi,\text{MC}} = \frac{r'_0{}^3}{(r'_0 + l \cos \alpha)^2 [(r'_0 + l \cos \alpha)^2 + (l \sin \alpha)^2]^{1/2}}. \quad (10)$$

The dashed lines in Figure 6 present $f_{k,\varphi,\text{MC}}$ as a function of l for $r'_0 = 1$ and different values of α . Comparing to the hydrodynamical case, at $l = 10$, $f_{k,\varphi,\text{MC}}$ decreases by a factor of ~ 77 for $\alpha = 70^\circ$, while for $\alpha = 10^\circ$ it decreases and by a factor of ~ 1300 !

We find then that $f_{k,\varphi,\text{MC}}$ is a much stronger function of l than $f_{k,\varphi}$. This indicates that an angular velocity conserving flow will become unvirialized much faster than an angular momentum conserving Keplerian flow.

We find that line-driven winds (Models 3 and 4) stay virialized over a long distance from the launching point, because they have an extended base of accelerating region in the poloidal wind. Any quantity weighted by density will be dominated by the contribution from this dense base. In Model 4, the inner region of the wind is particularly dense as it includes the failed wind (Proga et al. 2000; Proga & Kallman 2004).

Our analysis suggest that the flow will remain virialized under the following general conditions:

- The acceleration is vertical rather than radial (i.e., large α : see Figure 6).
- If α happens to be small, the flow better conserves the specific angular momentum rather than the angular velocity.
- The wind acceleration in the poloidal direction should be slow so that the wind base will be dense.

As expected, there are cases where winds are not virialized (e.g., Parker wind in Appendix A). However, if

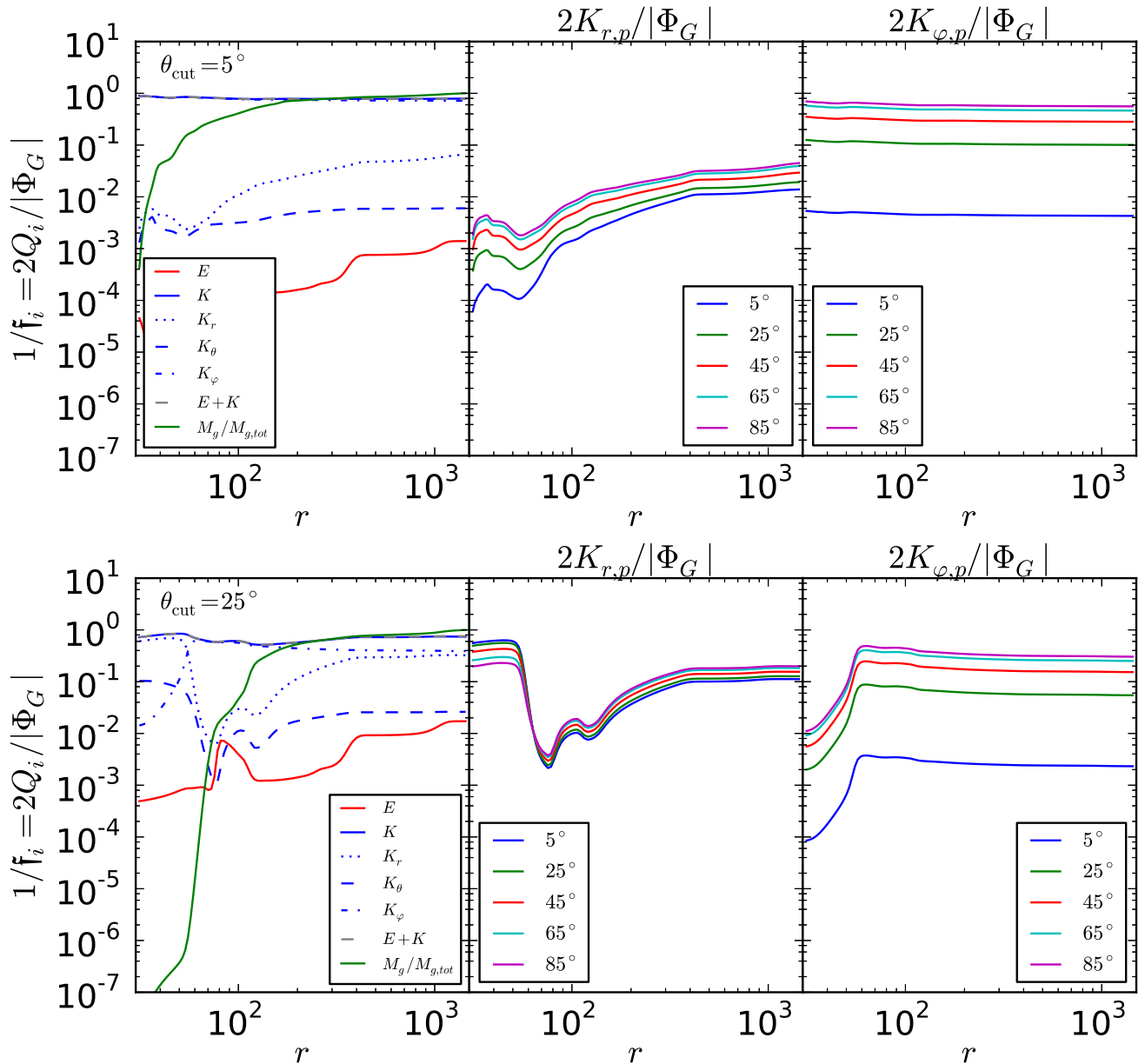


Figure 5. Same as Fig. 4, but with $\theta_{\text{cut}} = 5^\circ$ (top row), and $\theta_{\text{cut}} = 25^\circ$ (bottom row). We omit the disk in integration to emphasize the wind properties. We find that most of the mass is at low radii, and the wind is still virialized.

the wind is launched from a virialized system such as a Keplerian disk, the wind can appear as virialized to a distance greater than 10 times the launching radius (Figure 6). Therefore, our results support the assumption that the BLRs are virialized up to a large radius.

6. SUMMARY

The assumption that the BLRs are virialized is commonly used to determine the mass of SMBHs. While it is widely assumed that accreting gas is virialized, winds are often considered to be non-virialized as the non-gravitational forces break their connection to the central SMBH. In the present work, we analyze simulations of winds for four different cases, and show that the flow in the line-driven disk wind “remembers” its origin – a Keplerian disk – for a relatively long distance, and as such, can be considered to be virialized.

We also performed the same analysis for accretion/inflow simulations for all the models in Proga (2007) and Kurosawa & Proga (2009), covering a large range of parameter space (Eddington ratio, density, temperature, X-ray fraction and more), including models where thermal instability created dense cool clumps (cf., Barai et al. 2011, 2012; Moscibrodzka & Proga 2013). Generally, all inflows were found to be virialized because they are supersonic. As these results are similar to the above four simulations, we do not show them here.

We find that if the emission lines are generated close to the center, they would be observed as virialized up to a large radius. For a typical AGN with a SMBH of $10^8 M_\odot$, the flow would be virialized up to $\gtrsim 10^3 r_s$, where BLRs would be included. The projected quantities (the left panel of Figures 1c, 2c, 3c and 4c) show that $K_{\phi,p}$ dominates over $K_{r,p}$ even at small inclination angles, up

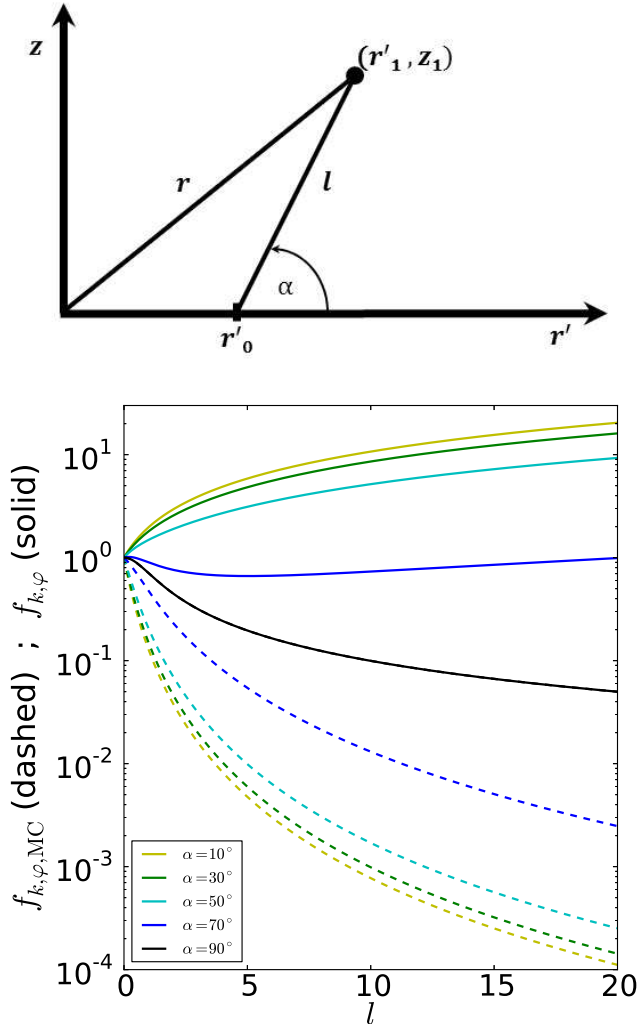


Figure 6. *Top panel:* Geometry of the calculation given in Section 5, and relevant parameters. *Bottom panel:* The rotational component $f_{k,\varphi}$ of the virial factor as a function of l for the specific angular momentum conserving wind (Eq. [9]; solid lines), and for the angular velocity conserving wind ($f_{k,\varphi,MC}$, Eq. [10]; dashed lines), for different values of α (see legend). The wind launching point is $r'_0 = 1$. Note that for $\alpha = 90^\circ$ the lines overlap for the two cases. A Keplerian flow becomes unvirialized slowly when the specific angular momentum is conserved, but much faster when the angular velocity is conserved.

to $\sim 20^\circ$ (for higher i $K_{r,p}$ becomes dominant). The implication of this is that the observed projected value of f will scale as $f \propto 1/\sin^2 i$ for $i \gtrsim 20^\circ$. As f_p and f relate to each other by density weighting and integration over volume, this implies that $f \propto 1/\sin^2 i$.

The average factor $\langle f \rangle$ discussed in the literature ranges from $\langle f \rangle = 1$ (McLure & Dunlop 2004), and ranging up to $\langle f \rangle = 4 - 6$ (Onken et al. 2004; Woo et al. 2010; Grier et al. 2013). Our Equation (7) is consistent with the result of Onken et al. (2004), who derived $f = 2 \ln 2 / \sin^2 i$, assuming a thin ring in Keplerian rotation. The dependency of $f \propto 1/\sin^2 i$ is indeed expected, as the flow in our simulations can be thought of as a collection of rings in Keplerian rotation. The numerical factor $2 \ln 2$ by Onken et al. (2004) comes from

relating the rotational velocity to the line velocity dispersion, while our numerical factor 1.32 ± 0.08 comes from density weighting and integration. Therefore we regard the numerical consistency as coincidental. We shall return to this point in a future paper where synthetic line profiles will be computed.

We note that other studies give different results for $f(i)$. For example, Decarli et al. (2008) suggested $f = (2c_1 \sin i + 2c_2/\sqrt{3})^{-1/2}$, where the parameters c_1 and c_2 quantify the importance of the disk and isotropic components of the BLR, respectively. For a thin disk $c_1 \rightarrow 1$ and $c_2 \rightarrow 0$, then $f \approx 1/\sqrt{2} \sin i$.

Theoretically, the uncertainty in the value of f is the source of error in the determination of SMBH masses. However, the theoretical value of f is not necessarily identical to the f -factor that is used in observational estimates. The latter depends on the particular way the line width is measured (e.g., whether FWHM or σ is used to determine the width, or how the line-width is determined for a profile with multiple peaks).

Furthermore, the BLR radius obtained by reverberation mapping is a weighted average, estimated from the cross-correlation lag between the changes of continuum and line response. In other words, the line width and the lag do not necessarily correspond to the same physical location (i.e., the line width does not necessarily give us the circular velocity at the radius obtained from the cross-correlation lag). We expect that there would be a simple relation between the theoretical value of f and the observed one, however, estimating this relationship accurately is beyond the scope of this paper.

We find that the line-driven disk wind models discussed here (Models 3 and 4) are virialized to a relatively large extent, although certainly there are classes of outflows that are not virialized (such as the Parker wind and Models 1 and 2). Our results support the notion that the BLR can be virialized even if it contains an outflow, provided that the outflow's structure is similar to that of a dense, slowly accelerating line-driven wind from a Keplerian disk.

This, in turn, gives additional support for a two component model (disk+line-driven disk wind) of the BLR in general and not just for the outflows in particular (see Chiang & Murray 1996, who arrived at a similar conclusion by considering only the disk and the wind base not the whole wind). Clearly it is necessary to continue to test this model. Our conclusions here motivate calculations of the reverberation response of a disk wind even if it is complex and time-dependent as in Model 4.

ACKNOWLEDGMENTS

We thank Alexei Baskin, Shai Kaspi, Julian Krolik, Ari Laor, Anna Pancoast, Stephen Rafter, Noam Soker, Timothy Waters and an anonymous referee for helpful comments. We acknowledge support provided by NASA through grants HST-AR-12835 and HST-AR-12150.01-A. from the Space Telescope Science Institute, which is operated by the Association of Universities for Research in Astronomy, Inc., under NASA contract NAS5-26555. This work was also supported in part by the NSF grant AST-0807491. Research by A.J.B. is supported by NSF

grant AST-1108835.

APPENDIX

A. BONDI ACCRETION AND PARKER WIND VIRIAL QUANTITIES

We demonstrate our analysis method on both Bondi accretion (Bondi 1952) and Parker winds (Parker 1965; see also Waters & Proga 2012 and references therein). The classic Bondi (1952) accretion scenario assumes a steady state where gas is in a radial flow with two forces acting on it: gravity and gas pressure. The flow is into a central point mass M , which is the only source of gravity. A steady accretion flow satisfies the Bernoulli equation

$$\frac{v^2}{2} + \int_{P_\infty}^P \frac{dP}{\rho} - \frac{GM}{r} = 0, \quad (\text{A1})$$

where v is the flow speed, G is the gravitational constant, and r is the radial distance from central object with mass M . The pressure P and the gas density ρ are assumed to be uniform at infinity with values P_∞ and ρ_∞ , respectively, and satisfy the polytropic equation of state $P/P_\infty = (\rho/\rho_\infty)^\gamma$, where γ is the adiabatic index. The speed of sound at infinity is $c_{s,\infty} = \sqrt{\gamma P_\infty/\rho_\infty}$. The Bernoulli equation with the above equation of state is then

$$\frac{v^2}{2} + \left(\frac{\gamma}{\gamma-1}\right) \frac{P_\infty}{\rho_\infty} \left[\left(\frac{\rho}{\rho_\infty}\right)^{\gamma-1} - 1 \right] - \frac{GM}{r} = 0. \quad (\text{A2})$$

The continuity equation gives the accretion rate $\dot{M} = \int r^2 \rho v d\Omega$. Under the spherical symmetry, $\dot{M} = 4\pi r^2 \rho v$. The solution gives the the Bondi accretion rate

$$\dot{M}_B = \frac{\lambda 4\pi G^2 M^2 \rho_\infty}{c_{s,\infty}^3}, \quad (\text{A3})$$

where the value of the constant λ determines the solution. A characteristic radius is also defined – the Bondi radius $R_B = GM/c_{s,\infty}^2$ – the distance from M where the forces are balanced.

Depending on the value of λ , a range of solutions are possible (Fig. 2 in Bondi 1952); the one relevant for astrophysical accretion is the so-called critical solution with the value of

$$\lambda_c = \left(\frac{1}{2}\right)^{\frac{(\gamma+1)}{2(\gamma-1)}} \left(\frac{5-3\gamma}{4}\right)^{\frac{(3\gamma-5)}{2(\gamma-1)}}. \quad (\text{A4})$$

For the critical solution, gas is subsonic in the outer parts, traverses a sonic point, and accretes onto the central object at a supersonic velocity. The second solution with the same value λ_c resembles a Parker wind. A supersonic inflow exists for $r < R_s/R_B = (5-3\gamma)/4$ if $\gamma < 5/3$, and there the gas is free falling. For a supersonic inflow, an analytic estimate is possible in the limit of $r \ll 1$.

We solve the classical 1D analytic solutions of the Bondi problem to find the density, velocity (and consequently the pressure and temperature) as a function of radius. We calculate the kinetic energy $k = v^2/2$, the gravitational potential due to the central mass $\phi_G = -GM/r$, and the specific enthalpy $h = \gamma e = (\gamma/\gamma -$

$1)P/\rho$, where e is the specific internal energy. We add a constant $-GM/[R_B(\gamma-1)]$ to the specific enthalpy to satisfy Equation A2. The above quantities are then presented in dimensionless units, taking $GM = 1$ (Fig. A1).

We calculate the density-weighted, volume-integrated quantities of the virial theorem as

$$Q_i = 4\pi \int_{r=0}^r q_i \rho r^2 dr, \quad (\text{A5})$$

where $q_i = (k, e, \phi_G)$ and $Q_i = (K, E, \Phi_G)$, respectively.

We apply the above calculation for Bondi accretion and Parker winds for different values of γ (Fig. A1). Taking the free-fall density and velocity, and substituting them into Eq. A5, we find that the free-fall limit gives $|\Phi_G|/2K = 0.5$. This is an expected result as a radial virialized inflow gives $f = 0.5$, and as long as both sides of the equation are weighted by the same density profile the result should remain unchanged.

REFERENCES

- Arav, N., Li, Z.-Y., & Begelman, M. C. 1994, *ApJ*, 432, 62
 Barai, P., Proga, D., & Nagamine, K. 2011, *MNRAS*, 418, 591
 Barai, P., Proga, D., & Nagamine, K. 2012, *MNRAS*, 424, 728
 Barth, A. J., Pancoast, A., Bennert, V. N., et al. 2013, *ApJ*, 769, 128
 Baskin, A., & Laor, A. 2005, *MNRAS*, 356, 1029
 Bentz, M. C., Horne, K., Barth, A. J., et al. 2010, *ApJ*, 720, L46
 Bentz, M. C., Walsh, J. L., Barth, A. J., et al. 2009, *ApJ*, 705, 199
 Blandford, R. D., & Begelman, M. C. 1999, *MNRAS*, 303, L1
 Blandford, R. D., & McKee, C. F. 1982, *ApJ*, 255, 419
 Blandford, R. D., & Payne, D. G. 1982, *MNRAS*, 199, 883
 Bondi, H. 1952, *MNRAS*, 112, 195
 Chiang, J., & Murray, N. 1996, *ApJ*, 466, 704
 Collin, S., Kawaguchi, T., Peterson, B. M., & Vestergaard, M. 2006, *A&A*, 456, 75
 Collin-Souffrin, S., Dyson, J. E., McDowell, J. C., & Perry, J. J. 1988, *MNRAS*, 232, 539
 Decarli, R., Labita, M., Treves, A., & Falomo, R. 2008, *MNRAS*, 387, 1237
 Denney, K. D. 2012, *ApJ*, 759, 44
 Denney, K. D., Pogge, R. W., Assef, R. J., et al. 2013, *arXiv:1303.3889*
 Faucher-Giguère, C.-A., & Quataert, E. 2012, *MNRAS*, 425, 605
 Font, A. S., McCarthy, I. G., Johnstone, D., & Ballantyne, D. R. 2004, *ApJ*, 607, 890
 Gaskell, C. M. 2010, *Accretion and Ejection in AGN: a Global View*, 427, 68
 Giustini, M., & Proga, D. 2012, *ApJ*, 758, 70
 Goad, M. R., Korista, K. T., & Ruff, A. J. 2012, *MNRAS*, 426, 3086
 Grier, C. J., Martini, P., Watson, L. C., et al. 2013, *arXiv:1305.2447*
 Hryniewicz, K., & Czerny, B. 2012, *Mem. Soc. Astron. Italiana*, 83, 146
 Kallman, T. R., Wilkes, B. J., Krolik, J. H., & Green, R. 1993, *ApJ*, 403, 45
 Kaspi, S., Smith, P. S., Netzer, H., et al. 2000, *ApJ*, 533, 631
 Kollatschny, W. 2003, *A&A*, 407, 461
 Kollatschny, W., & Zetzl, M. 2013, *A&A*, 551, L6
 Konigl, A., & Kartje, J. F. 1994, *ApJ*, 434, 446
 Krolik, J. H. 2001, *ApJ*, 551, 72
 Kurosawa, R., Proga, D., & Nagamine, K. 2009, *ApJ*, 707, 823
 Kurosawa, R., & Proga, D. 2009, *MNRAS*, 397, 1791
 Laor, A., Barth, A. J., Ho, L. C., & Filippenko, A. V. 2006, *ApJ*, 636, 83
 Leighly, K. M. 2004, *ApJ*, 611, 125
 Luketic, S., Proga, D., Kallman, T. R., Raymond, J. C., & Miller, J. M. 2010, *ApJ*, 719, 515
 Marconi, A., Axon, D. J., Maiolino, R., et al. 2008, *ApJ*, 678, 693
 McLure, R. J., & Dunlop, J. S. 2004, *MNRAS*, 352, 1390
 Mościbrodzka, M., & Proga, D. 2013, *ApJ*, 767, 156
 Murray, N., Chiang, J., Grossman, S. A., & Voit, G. M. 1995, *ApJ*, 451, 498
 Nicastro, F. 2000, *ApJ*, 530, L65
 Onken, C. A., Ferrarese, L., Merritt, D., et al. 2004, *ApJ*, 615, 645
 Onken, C. A., & Peterson, B. M. 2002, *ApJ*, 572, 746

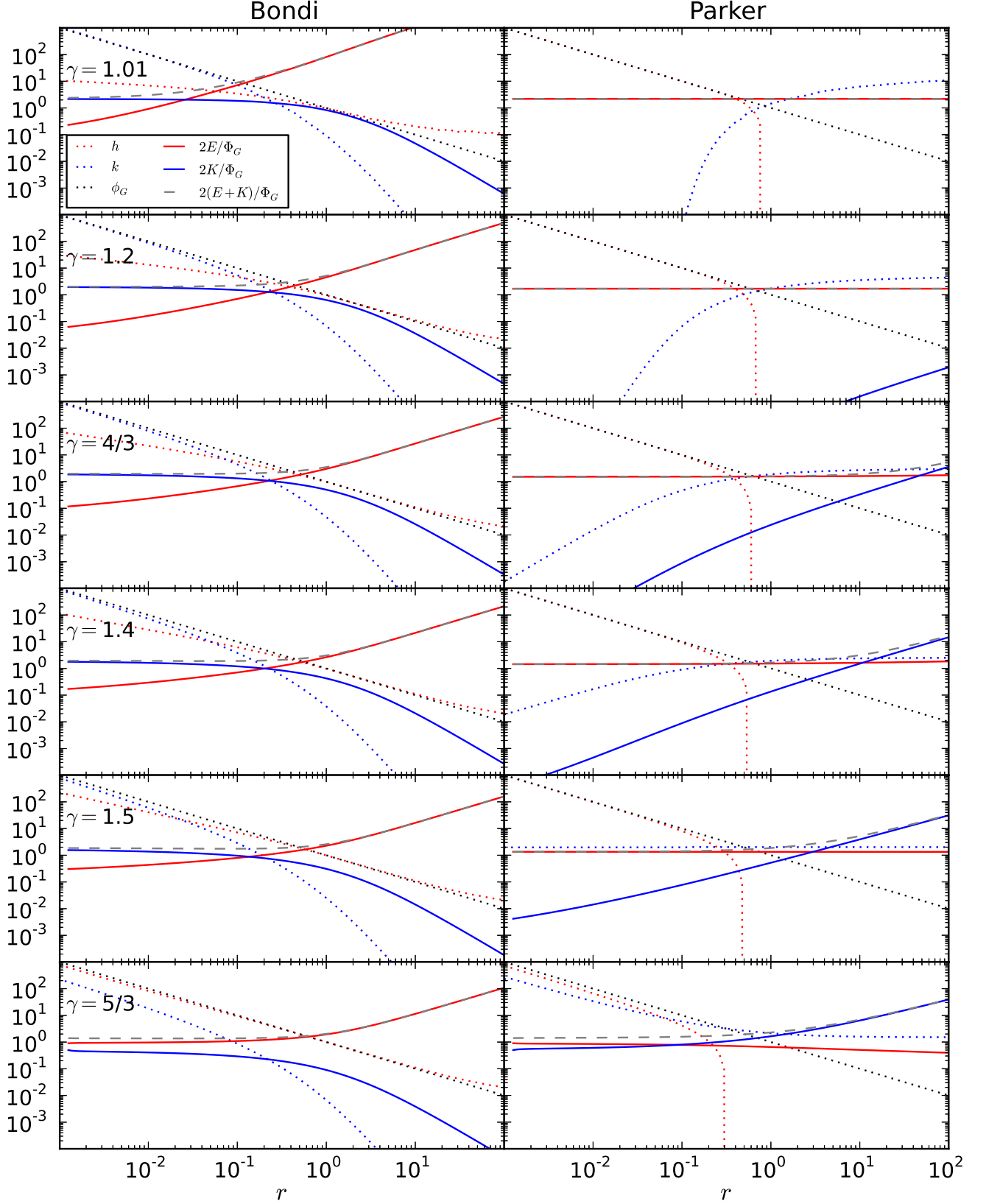


Figure A1. *Left panels:* Dotted lines show the specific kinetic energy k , specific enthalpy h , and gravitational potential ϕ_G , calculated by solving the 1D Bondi accretion problem. Solid lines are the density-weighted, volume-integrated quantities Q_i of the virial theorem: kinetic energy (K), enthalpy E , and gravitational potential Φ_G . Plotted are the ratios $f_i^{-1} = 2Q_i/|\Phi_G|$. *Right panels:* Same as the left panels, but for the Parker wind solution.

- Pancoast, A., Brewer, B. J., & Treu, T. 2011, *ApJ*, 730, 139
Parker, E. N. 1965, *Space Sci. Rev.*, 4, 666
Peterson, B. M. 1993, *PASP*, 105, 247
Peterson, B. M. 2001, *Advanced Lectures on the Starburst-AGN*, 3
Peterson, B. M., Ferrarese, L., Gilbert, K. M., et al. 2004, *ApJ*, 613, 682
Peterson, B. M., & Wandel, A. 1999, *ApJ*, 521, L95
Peterson, B. M., & Wandel, A. 2000, *ApJ*, 540, L13
Proga, D. 2003, *ApJ*, 592, L9
Proga, D. 2007, *ApJ*, 661, 693
Proga, D., & Kallman, T. R. 2002, *ApJ*, 565, 455
Proga, D., & Kallman, T. R. 2004, *ApJ*, 616, 688
Proga, D., Stone, J. M., & Drew, J. E. 1998, *MNRAS*, 295, 595
Proga, D., Stone, J. M., & Drew, J. E. 1999, *MNRAS*, 310, 476
Proga, D., Stone, J. M., & Kallman, T. R. 2000, *ApJ*, 543, 686
Proga, D., Ostriker, J. P., & Kurosawa, R. 2008, *ApJ*, 676, 101
Proga, D., & Begelman, M. C. 2003, *ApJ*, 582, 69
Richards, G. T., Kruczek, N. E., Gallagher, S. C., et al. 2011, *AJ*, 141, 167
Roth, N., Kasen, D., Hopkins, P. F., & Quataert, E. 2012, *ApJ*, 759, 36
Shen, Y. 2013, *Bulletin of the Astronomical Society of India*, 41, 61
Sim, S. A., Proga, D., Miller, L., Long, K. S., & Turner, T. J. 2010, *MNRAS*, 408, 1396
Ulrich, M.-H., Maraschi, L., & Urry, C. M. 1997, *ARA&A*, 35, 445
Wang, H., Wang, T., Zhou, H., et al. 2011, *ApJ*, 738, 85
Waters, T. R., & Proga, D. 2012, *MNRAS*, 426, 2239
Watson, L. C., Mathur, S., & Grupe, D. 2007, *AJ*, 133, 2435
Woo, J.-H., Treu, T., Barth, A. J., et al. 2010, *ApJ*, 716, 269